MOF-derived Co/ZnO/C nanocomposites with excellent microwave absorption properties

Longlong Qin[1], Biao Zeng[1], Ting Qin[1], Chen Li[1], Chao Tang[1], Shengxiang Huang[1], and Lianwen Deng[1,*] (ID)

[1] School of Physics and Electronics, Central South University, Changsha 410083, China

ABSTRACT

Magnetic nanoparticles combined with semiconductive metal oxides are considered to be ideal candidates for electromagnetic wave absorption materials, benefiting from suitable conductivity, matched magnetism and strong polarization. In this work, Co–ZnO binary MOF (ZIF-67, ZIF-8)-based carbon composites were fabricated via a facile synthesis route. After optimization of composition and technological parameters, the synthesized nanocomposites acquired optimal electromagnetic characteristics and exhibited superb microwave absorption ability. The lowest reflection loss of the Co–ZnO–C-800 sample reached − 44.8 dB at 9.2 GHz with a thickness of 2.9 mm, and the effective absorption bandwidth (EAB) was 6.95 GHz (6.59–13.54 GHz). The microwave loss mechanism of the nanocomposite material mainly involved dielectric loss and magnetic resonance absorption. This work provides an ingenious design and synthesis strategy for novel lightweight electromagnetic wave absorbers with broadband EAB and strong absorption.

1 Introduction

With dramatic development of electronic devices and communication equipment, electromagnetic pollution has become a nonnegligible issue affecting our ecological environment. To address the issue, microwave-absorbing materials (MAMs) are highly desired [1–3]. It has been widely accepted that MAMs with broad effective absorption band (EAB) and thin matching thickness is an efficient strategy to solve the electromagnetic pollution problem [4–7].

More recently, metal-organic frameworks (MOFs) materials, formed by coordination of the metal ions and organic groups, have aroused extensive attention on account of their light weight, specific surface area and adjustable structure [8–11]. The pyrolysis process of MOFs in inert gases will form porous carbon matrix with stable chemical properties and different morphologies, which is beneficial to synthesizing high-performance MAMs. It is worth noting that the porous carbon matrix can be further optimized by combining with metal components to enhance microwave absorption ability, such as, magnetic (Fe, Co, Ni)-MOFs, non-magnetic (Zn, Cu, Ti)-MOFs, and multi-magnetic alloy (CoNi–FeNi–FeCo) MOFs [12]. Liu et al. synthesized the Ni particle with special rod-

like morphology by pyrolysis of the Ni-based MOFs. After carbonizing at 600 °C, the Ni/C composite presented lowest reflection loss (RL_{min}) of − 51.8 dB and EAB of 3.48 GHz at the matching thickness of 2.6 mm and filler ratio of 40 wt% [13]. Zhao et al. obtained hierarchically hollow porous carbon microcubes (HPCMC) from ZIF-67@SiO$_2$ composites, The SiO$_2$ layer could prevent shrinkage of MOFs precursors during the pyrolysis process. After subsequent HF etching, HPCMC was synthesized. The RL_{min} reached − 60.7 dB with the matching thickness of 3.2 mm, and EAB up to 14.4 GHz (3.6–18 GHz) [14]. For multi-magnetic metal MOFs, Wei et al. reported a facile mass ratio regulating of ZIF-67/PFC and thermal annealing approach to prepare the hollow CoFe@C nanocomposites, presenting RL_{min} of − 44.1 dB and EAB of 5.2 GHz at the matching thickness of 2.3 mm [15].

However, there are few reports of magnetic and non-magnetic binary MOFs-based nanocomposites as MAMs. If it is possible to insert non-magnetic semiconductors combined with magnetic components in the porous carbon matrix, based on the hetero-interfaces between magnetic component and semiconductor, it can be expected to improve microwave absorption performance by optimizing impedance matching and strengthening polarization process [16].

Herein, magnetic cobalt/zinc oxide/porous carbon (Co–ZnO–C) composites were synthesized via a facile dissolution technology. After pyrolysis at different temperatures, Co–ZnO–C with different microwave absorption performances were obtained. To verify the excellent performance of the designed MAMs, morphology, element composition and electromagnetic parameters were analyzed. This study may pave the way for designing microwave absorbers with lightweight and excellent microwave absorption performance.

2 Experiment

2.1 Raw and auxiliary materials

N,N-dimethyformanide (C$_3$H$_7$NO, DMF, A.R.), PAN powder [(C$_3$H$_3$N)$_n$, Mw:150000], and hydrous methanol are from Aladdin Chemical Reagent Co.,Ltd. Cobalt nitrate hexahydrate [Co(NO$_3$)$_2$.6H$_2$O, 99.9%], zinc nitrate hexahydrate [Zn(NO$_3$)$_2$.6H$_2$O, 99.9%], and 2-methylimidazole (MeIM, 98%) are from Sinopharm Chemical Reagent Co.,Ltd. All of the

chemicals are commercially available and can be used directly. Deionized water and ethanol are used in the cleaning process.

2.2 Preparation of Co–ZnO–C

The Co–ZnO–C composites were synthesized through the facile dissolution process, as shown in Fig. 1 [17]. PAN powder (1 g) was dissolved in DMF (9.5ml) solvent, followed by the addition of MeIM (0.35 g), and being stirred magnetically for 10 h. Then, Zn(NO$_3$)$_2$.6H$_2$O (0.3 g), Co(NO$_3$)$_2$.6H$_2$O (0.58 g), and hydrous methanol (15 ml) were added into the above solution and kept for 24 h at room temperature. The products were washed with methanol four times, and dried at 40 °C in vacuum drying furnace for 10 h. Then, ZIF-8/ZIF-67 precursor was obtained. The above products were placed in a ceramic boat and heated in different temperatures (600,700,800,900 °C) for 3 h under argon atmosphere. After being annealed for 6 h, the final black powders were named as Co–ZnO–C-T (600,700,800,900 °C) and experienced subsequent characterization and measurements.

2.3 Characterization

The crystal structure of Co–ZnO–C was analyzed by X-ray diffraction (XRD, D8 ADVABCE Da Vinci) using Cu Kα radiation (λ = 1.54 Å). X-ray photoelectron spectroscopy (XPS, Thermofisher-VG Scientific, ESCALAB 250Xi spectrometer) were used to investigate the combined valance state of each element. Raman spectra (Renishaw, UK) was employed to verify the defects and graphitization degree in the carbon matrix. Field emission scanning electron microscopy (FE-SEM, Hitachi S480) was adopted to observe micromorphology. To compare the absorption performances of the samples, the coaxial samples were made by paraffin with the same filler ratio of 20%. The electromagnetic parameters were measured by the vector network analyzer (VNA, Agilent N5230A) in the frequency range of 2–18 GHz.

3 Results and discussion

The crystal structures of Co–ZnO–C were measured by XRD. As shown in Fig. 2a. Obviously, all the samples present the same diffraction peak at 26.0°,

Fig. 1 Schematic illustration of the fabrication process of Co–ZnO–C
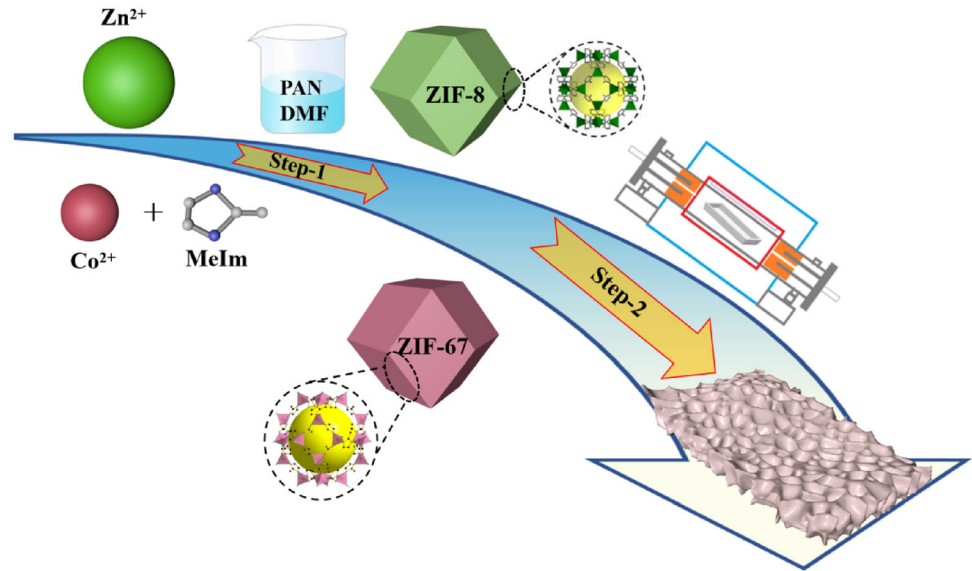
attributing to (0 0 2) plane of the graphite carbon (PDF # No. 26-1076) which converted from PAN [18–20]. The diffraction peaks at 44.2°, 51.6° and 76.0°, correspond to (1 1 1), (2 0 0) and (2 2 0) planes of the face-centered cubic metallic cobalt (PDF # No. 15–0806), respectively [21–23]. The inconspicuous peak at 36.2° could be identified as (1 0 1) plane of zinc oxide [24–26]. Notably, when the pyrolysis temperature increases, the crystallization degree of Co–ZnO–C becomes clear. No other diffraction peaks of Co and ZnO are observed in the Co–ZnO–C-800 and Co–ZnO–C-900 samples, proving that after pyrolysis at high temperature in inert atmosphere, ZIF-8/ZIF-67 transfer to crystalline Co and ZnO, and embedded in the carbon matrix.

Raman spectroscopy is employed to evaluate the degree of graphitization and defects in the samples. The D band (1335–1344 cm^{-1}) and G band (1581–1590 cm^{-1}) are ascribed to the defective structures of sp^3 carbon atoms and graphitic grid of sp^2 carbon atoms, respectively [6, 27, 28]. The intensity ratio of D-band to G-band (I_D/I_G) is generally used to evaluate the degree of graphitization in carbon-based MAMs. As shown in Fig. 2b, the I_D/I_G ratios of Co–ZnO–C-(600–900) are 1.32, 1.02, 0.89, and 0.91, respectively. To analyze the defect degree of the prepared Co–ZnO–C, the relevant average distance between point defects (L_d) and defect density (n_d) is calculated by the Eqs. (1) and (2) [14, 29, 30].

$$L_d(nm) = \sqrt{(1.8 \pm 0.5) \times 10^{-9} \times \lambda_L^4 \times \left(\frac{I_D}{I_G}\right)^{-1}} \quad (1)$$

$$n_d(cm^{-2}) = (1.8 \pm 0.5) \times 10^{28} \times \lambda_L^{-4} \times \frac{I_D}{I_G} \quad (2)$$

λ_L stands for the excitation laser wavelength. It is obvious that the pyrolysis temperature plays an important role to the porous structure and graphitization degree of the materials. As shown in Fig. 2d, Co–ZnO–C-800 has the lowest (L_d) and highest (n_d) values, representing appropriate porous structure and graphitization degree.

Morphology and micro-structure of the prepared Co–ZnO–C nanocomposites are observed by SEM. As presented in Fig. 3a, b, the rhomboid decahedron MOFs particles disperse uniformly in the carbon matrix, the residual organic components will decrease the dielectric properties of materials. To resolve the organic components of ZIF-8 and ZIF-67, the pyrolysis temperature is increased. As shown in Fig. 3c, d, the MOFs organic components almost disappear after pyrolysis at 800 °C and 900 °C, thus the porous structures formed.

X-ray photoelectron spectroscopy (XPS) is used to detect the chemical composition of Co–ZnO–C-800. Figure 4a is the full scan spectrum of the sample, revealing elements of C, N, O, Co, and Zn in Co–ZnO–C-800. As shown in Fig. 4b, the narrow scan C
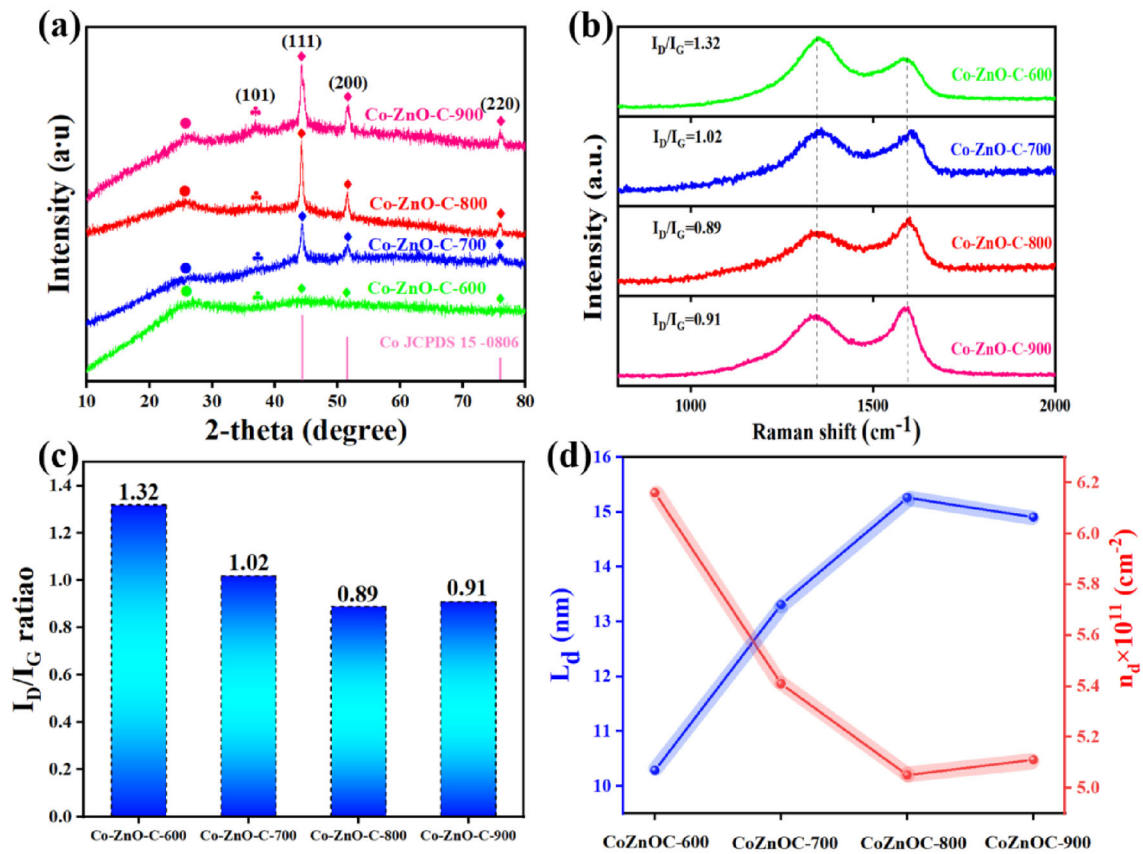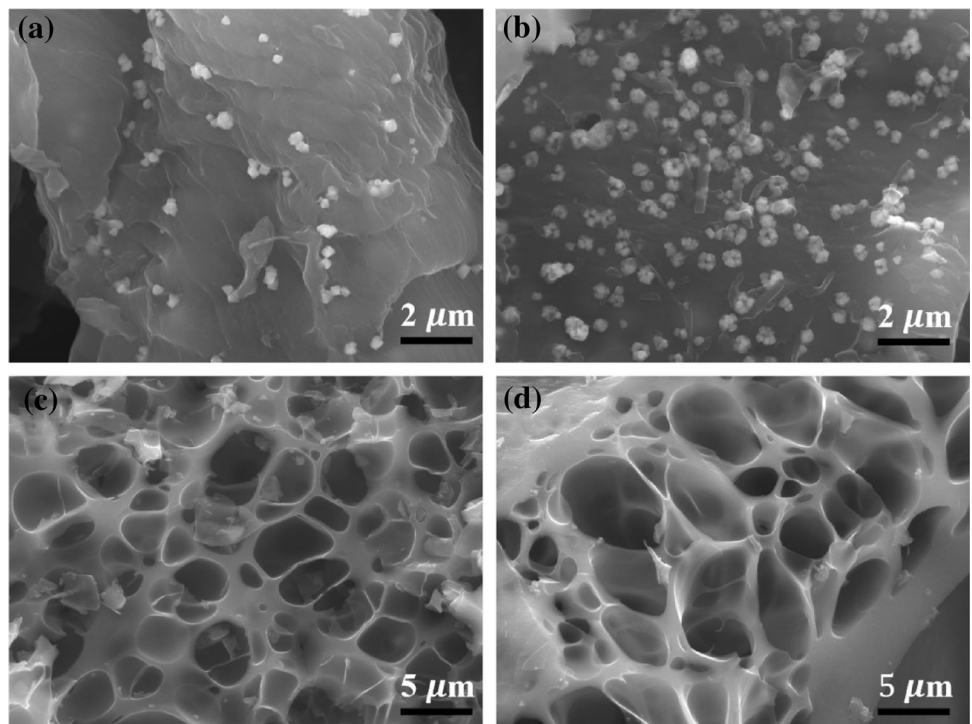
Fig. 2 **a**: XRD patterns; **b**: Raman spectra; **c**: I_D/I_G value; **d**: L_d and n_d of Co–ZnO–C

Fig. 3 SEM images of: **a**: Co–ZnO–C-600; **b**: Co–ZnO–C-700; **c**: Co–ZnO–C-800; **d**: Co–ZnO–C-900

1s spectrum exhibits three feature peaks corresponding to C–C at 283.8 eV, C=N at 285.4 eV, and C–O at 286.6 eV [31], respectively. The characteristic peaks of N 1s appear at 397.2 eV, 397.8 eV, and 399.2 eV, corresponding to pyridinic N, pyrrolic N, and graphitic N, indicating N atoms embedded in carbon network, as shown in Fig. 4c [32, 33]. Notably, the electronegativity of pyridinic N and pyrrolic N will induce strong coupling with adjacent C, and improve the dipole polarization loss greatly [34]. The XPS spectra of Zn 2p present two peaks at 1021 eV (2p3/2), 1044 eV(2p1/2) [34]. In Fig. 4d, the binding energy of O 1s can be deconvolved into O^{2-}(ZnO) at 530 eV, C=O at 531.1 eV, C–O at 532.6 eV, revealing the oxygen vacancy formed in the pyrolysis process [34]. The residual oxygen containing polar groups synergizes with multi-site vacancy, acting as the polarization center of dipole, and benefiting to loss of electromagnetic wave. O^{2-}(ZnO) at 530 eV also proves existence of ZnO [35]. As shown in Fig. 4f, the Co 2p XPS spectra present two pairs of (2p3/2)(2p1/2) doublets for metallic Co (777.9/795.5 eV), Co–C (782/796.7 eV), and Co–Nx (785.7/802.2 eV) [36].

The EMA performances of the as-prepared samples are evaluated through values of the microwave reflection loss (RL) [37]. RL is calculated using the Eq. (3).

$$R_L = 20\lg \frac{|Z_{in} - Z_0|}{|Z_{in} + Z_0|} \tag{3}$$

The normalized input impedance (Z_{in}) is given by Eq. (4).

$$Z_{in} = Z_0 \sqrt{\frac{\mu_r}{\epsilon_r}} \tanh \left[j\frac{2\pi}{c} \sqrt{\mu_r \epsilon_r} fd \right] \tag{4}$$

where Z_0 is impedance of the free space, f is the frequency, c is the light speed, and d is the thickness of the absorbent materials. ϵ_r is the complex permittivity, $\epsilon_r = \epsilon' - j\epsilon'$, μ_r is the complex permeability, $\mu_r = \mu\prime - j\mu\prime\prime$. For practical applications, a large effective absorption bandwidth (EAB, the frequency range for RL ≤ -10 dB) is also required [38]. Figure 5 shows the RL curves of the four prepared samples in 2–18 GHz. It is notable that Co–ZnO–C-600 and Co–ZnO–C-700 exhibit relatively poor microwave absorption with RL around −6 dB due to the
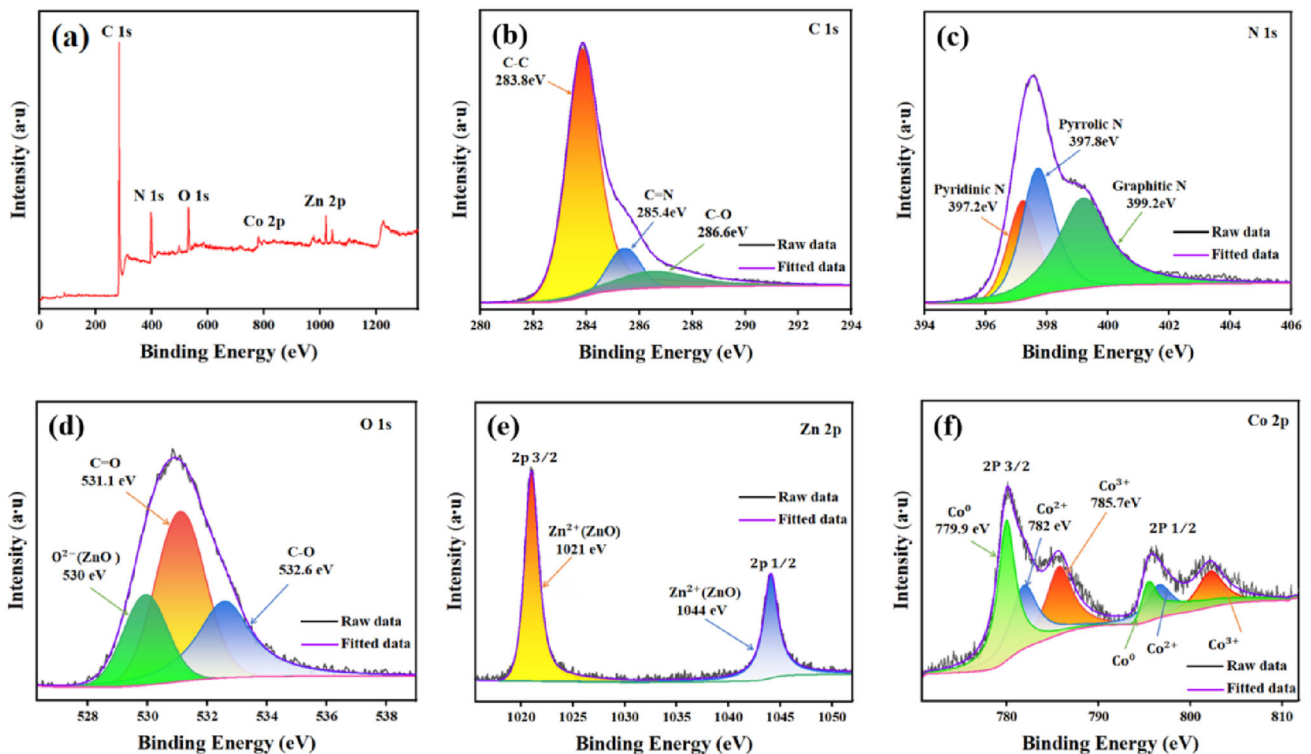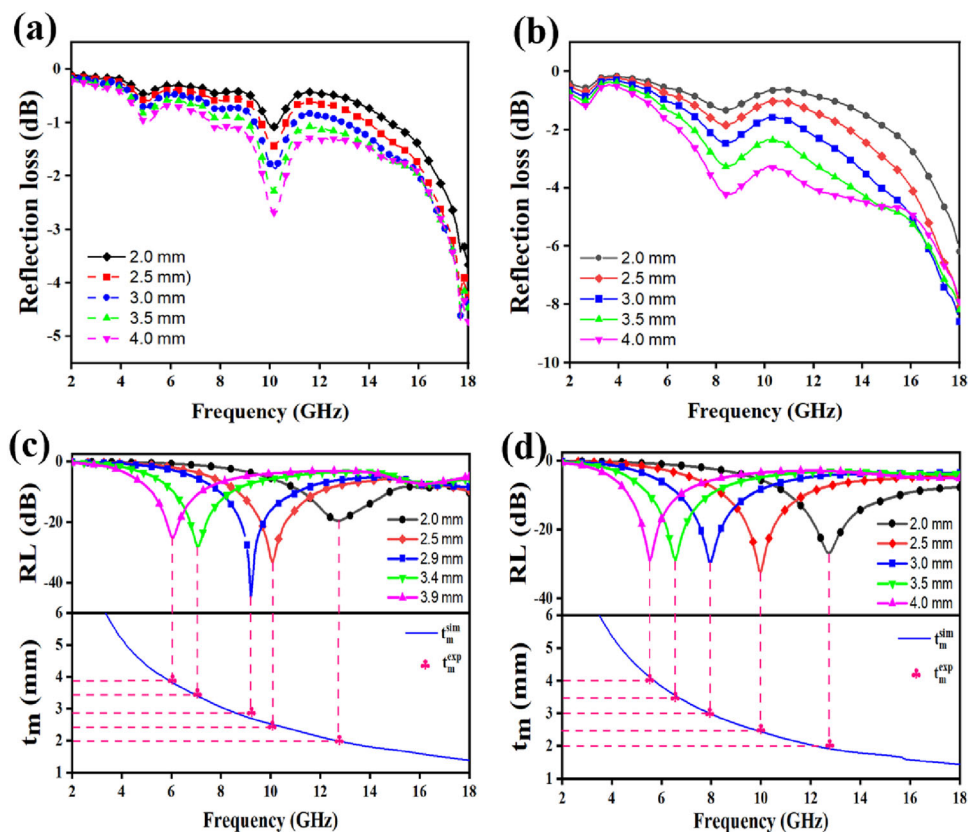

Fig. 4 XPS of Co–ZnO–C-800: **a**: full scan; **b**: C 1s XPS spectrum; **c**: N Is XPS spectrum; **d**: O 1 S XPS spectrum; **e**: Zn 2p XPS spectrum; **f**: Co 2p XPS spectrum

Fig. 5 RL curves for: **a**: Co–ZnO–C-600; **b**: Co–ZnO–C-700. Simulations of the absorber thickness (t_m) versus peak frequency (f_m) for: **c**: Co–ZnO–C-800; **d**: Co–ZnO–C-900

incomplete pyrolysis of ZIF-8/ZIF-67. The highest RL value of Co–ZnO–C-800 is − 44.8 dB at 9.2 GHZ. In addition, 3D presentation of the theoretical RL values in various thickness (2–4 mm) are calculated for Co–ZnO–C-800 and Co–ZnO–C-900. As shown in Fig. 6, when thickness increases, the corresponding lowest RL value of Co–ZnO–C-800 and Co–ZnO–C-900 all shift to the low frequency band, which can be well explained by the Eq. (5) [39].

$$t_m = n\lambda/4 = nc/[(4f_m)(|\varepsilon_r||\mu_r|)^{1/2})] \quad (n = 1, 3, 5...) \quad (5)$$

where t_m and f_m are the matching thickness and matching frequency, respectively. As shown in Fig. 5c, d, the experimental t_m values (t_m^{exp}) are in good coincidence with the simulated thickness (t_m^{sim}), indicating strong microwave dissipation at matching thickness and specific frequency [40].

It is found that the EMA performances of Co–ZnO–C MAMs are improved when the pyrolysis temperature increases from 700 °C to 800 °C and deteriorate when the temperature surpasses 900 °C. Obviously, the Co–ZnO–C-800 sample shows the best EMA performance, the RL peak value reaches − 44.8 dB at

9.2 GHz with a matching thickness of 2.9 mm, and corresponding EAB reaches 6.95 GHz.

The EM wave loss is directly related to the complex permittivity ($\epsilon = \epsilon\prime - j\epsilon\prime\prime$) and permeability ($\mu = \mu\prime - j\mu\prime\prime$) [41]. The loss tangent ($\tan\delta_\epsilon = \epsilon\prime\prime/\epsilon\prime, \tan\delta_\mu = \mu\prime\prime/\mu\prime$) is used to evaluate the efficiency of conversion for the incident electromagnetic energy to heat or other energy. As shown in Fig. 7, Co–ZnO–C-(600/700) possess the lower values of $\epsilon\prime$, $\epsilon\prime\prime$ and $\tan\delta_\epsilon$ in 2–18 GHz, relating to incomplete carbonization of MOFs in low temperature. When the pyrolysis temperature increases, $\epsilon\prime$, $\epsilon\prime\prime$ and $\tan\delta_\epsilon$ all step up in 2-18 GHz. In addition, for Co–ZnO–C-(800/900), $\epsilon\prime\prime$ and $\tan\delta_\epsilon$ present similar increased tendency from 8 to 18 GHz, indicating typical frequency dispersion behavior, and commonly occurred in carbon-based MA materials [42]. when EW propagates into the porous structure, charges accumulated on the boundary will cause strong interface polarization. Some resonant peaks appear in $\epsilon\prime\prime$ spectra, demonstrating the multiple polarization relaxation, such as interfacial polarization and dipole polarization in the composites.
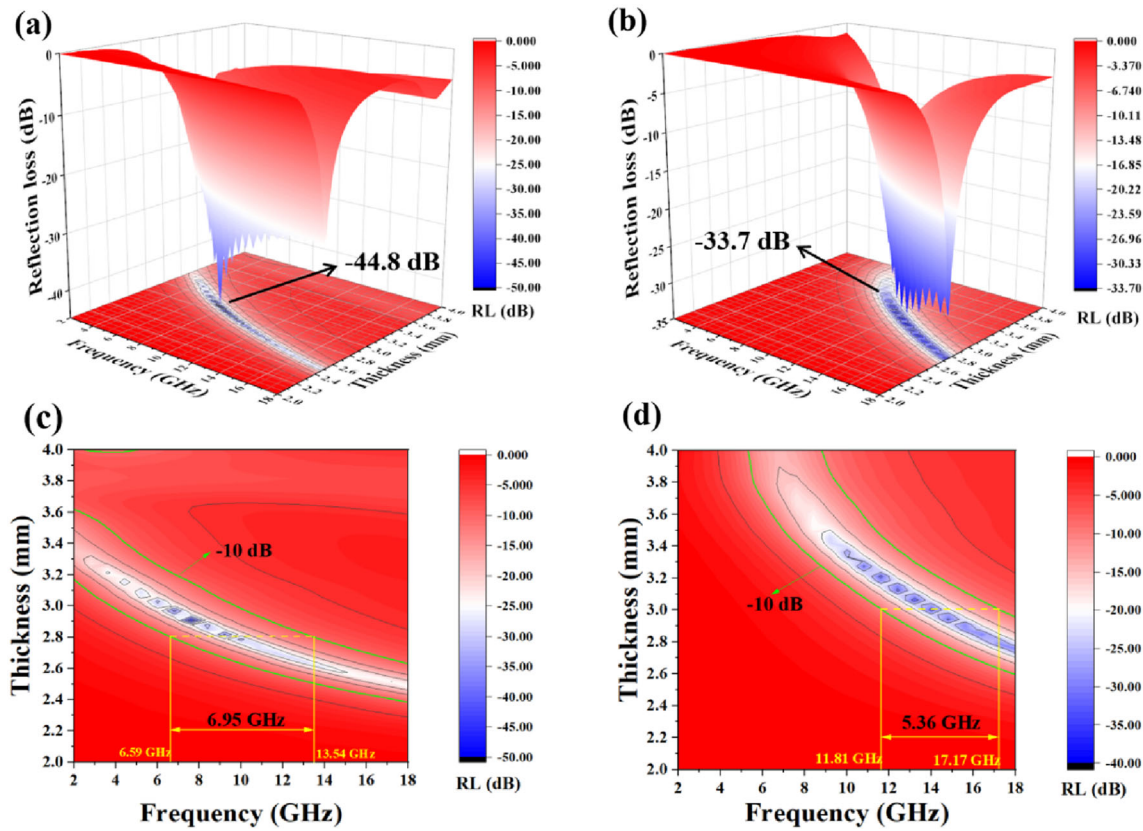
Fig. 6 3D presentation for **a**: Co–ZnO–C-800; **b**: Co–ZnO–C-900. and 2D projection images of RL for **c**: Co–ZnO–C-800; **d**: Co–ZnO–C-900

The permeability spectra of Co–ZnO–C are shown in Fig. 7d and e. The complex permeability of Co–ZnO–C-(800/900) shows downward trend with increasing frequency, implying that Co–ZnO–C comply with the Snoek's limit in the microwave range [43]. Usually, the magnetic loss originated from natural resonance, exchange resonance and eddy current. The natural resonance is related to shape anisotropy and magnetic crystal anisotropy, thus natural resonance plays a predominant role in magnetic loss. Based on Aharoni theory, the exchange resonance frequency is described by the Eq. (6) [44].

$$f_{exc} = \left(H_0 - aM_s + \gamma H_a + c \cdot \frac{u_{kn}^2}{R^2 M_s}\right)\gamma/2\pi \tag{6}$$

where R is the radius of the magnetic particle, H_0 is the magnetic crystalline anisotropy field. From above theory, for the magnetic nanocomposites, f_{exc} will shift towards high frequency when the particle size decreases.

When electromagnetic wave incident on the surface of conductive absorber, the induced eddy current will produce strong dissipation to the electromagnetic energy. The eddy current loss is determined by conductivity (σ) and thickness (d) of the absorber, and can be expressed by Eq. (7):

$$C_0 = 2\pi\mu_0 d^2 \sigma = \mu''(\mu')^{-2} f^{-1} \tag{7}$$

As shown in Fig. 7h, C_0 declines firstly and then remains stable when the frequency increases from 8 to 16 GHz, demonstrating the eddy current loss occurred at this frequency range [45].

The attenuation constant α is used to evaluate the microwave loss capacity, as expressed by Eq. (8) [46]:

$$\alpha = \frac{\sqrt{2}\pi f}{c} \times \sqrt{(\mu''\epsilon'' - \mu'\epsilon') + \sqrt{(\mu''\epsilon'' + \mu'\epsilon')^2 + (\mu''\epsilon' - \mu'\epsilon'')^2}} \tag{8}$$

In Fig. 7(g), α of Co–ZnO–C-800 is much larger than others in 2–18 GHz, indicating strong microwave attenuation loss ability.

The Co–ZnO–C(800 °C/900 °C) nanocomposites exhibit excellent microwave absorption performances, it's closely related to the dielectric behaviors.
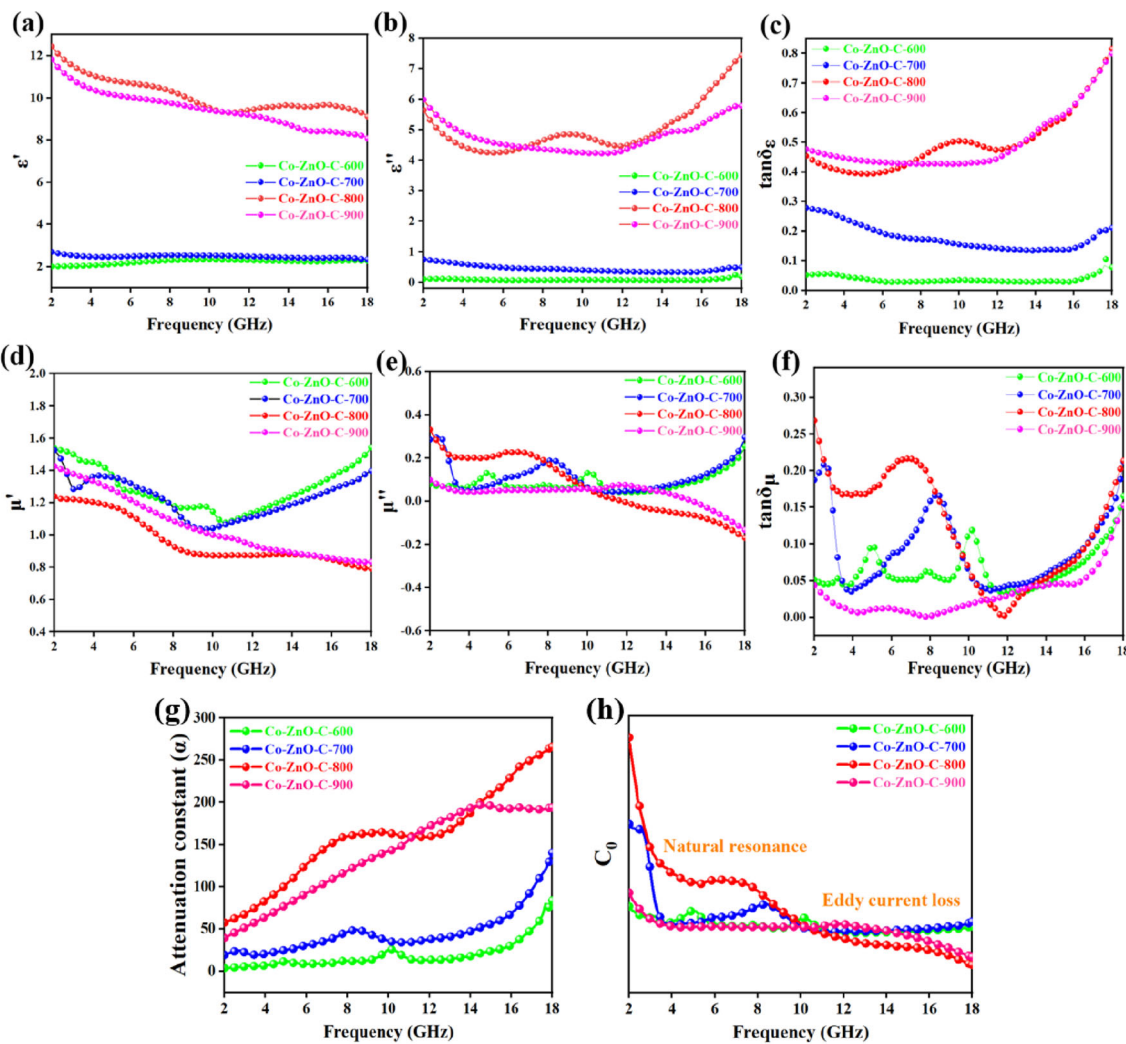
Fig. 7 **a–f**: Electromagnetic parameters **g**: attenuation constant; **h**: eddy current coefficient of Co–ZnO–C-600, 700, 800, 900

And the relationship between $\epsilon\prime$ and $\epsilon\prime\prime$ can be described by the Debye theory, and can be expressed by Eqs. (9) and (10) [47].

$$\epsilon\prime = \epsilon_\infty + \frac{\epsilon_s - \epsilon_\infty}{1 + w^2\tau^2} \qquad (9)$$

$$\epsilon\prime\prime = \frac{w\tau(\epsilon_s - \epsilon_\infty)}{1 + w^2\tau^2} + \frac{\sigma}{\epsilon_0 w} = \epsilon_p'' + \epsilon_c'' \qquad (10)$$

where w is angular frequency, ϵ_0 is permittivity constant in vacuum, ϵ_∞ is relative dielectric permittivity at the high-frequency limit, ϵ_s is static permittivity, and τ is polarization relaxation time which is the crucial factor in the dielectric process. The first part in the above formula (10) represents the polarization loss, the second part is conductive loss. Equations (9) and (10) are combined and simplified as shown in Eq. (11) [47].

$$\left(\varepsilon\prime - \frac{\varepsilon_\infty + \varepsilon_s}{2}\right) + (\varepsilon\prime\prime)^2 = \left(\frac{\varepsilon_\infty - \varepsilon_s}{2}\right)^2 \qquad (11)$$

The fluctuation of the complex permittivity manifests the polarization relaxation process, it's usually representing as a distorted semicircle in the $\epsilon\prime - \epsilon\prime\prime$-plot. Considering conductive loss in the carbon-based nanocomposites, the $\epsilon\prime - \epsilon\prime\prime$ curve will extend to the upper right of the coordinate axis. As shown in Fig. 8a, b, the two samples present three relaxation stages, induced by the oxygen vacancy defect, discontinuous graphite region and functional groups(C–O, C=O, etc.). Comparison of polarization loss ϵ_p'' with conductance loss ϵ_c'' are shown in Fig. 8c, d.

To prove that appropriate conductivity can result in strong conductive loss, we have used simulation
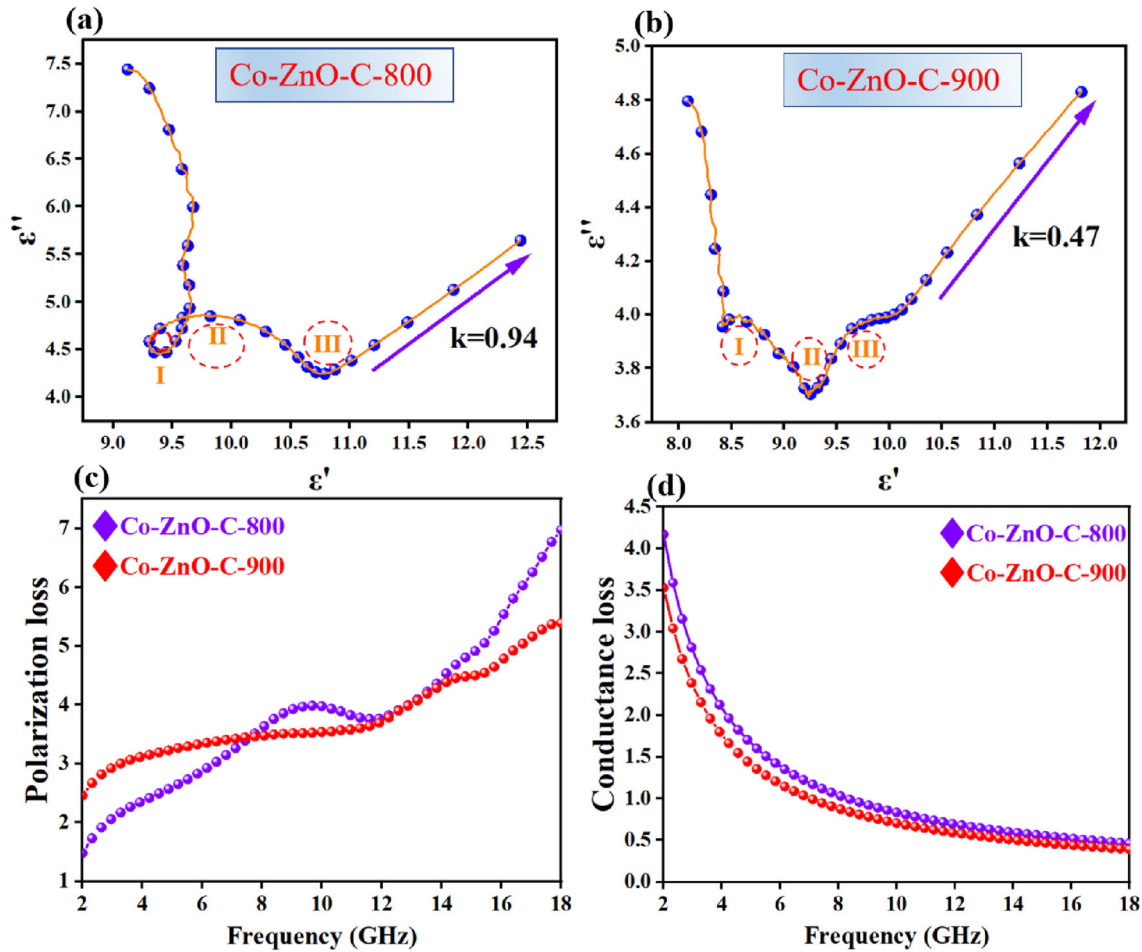
Fig. 8 **a**: Cole–Cole curve of Co–ZnO–C-800; **b**: Cole-Cole curve of Co–ZnO–C-900; **c, d**: polarization loss and conductance loss of Co–ZnO–C-800 and Co–ZnO–C-900

calculations and experimental tests to analyze the conductivity of Co–ZnO–C. The long straight line in Cole–Cole plots was chosen as a data fitting object, and so on with three other samples. As shown in Fig. 9, The values of σ for Co–ZnO–C-600, Co–ZnO–C-700, Co–ZnO–C-800 and Co–ZnO–C-900 are 0.12, 0.22, 0.26 and 0.25 S/m, respectively. We measured the conductivity of the Co–ZnO–C samples using the four-probe method. All the samples were tested four times and then averaged. The measured values of conductivity for Co–ZnO–C-600, Co–ZnO–C-700, Co–ZnO–C-800 and Co–ZnO–C-900 are 0.17, 0.24, 0.32 and 0.29 S/m, respectively. Co–ZnO–C-800 has the largest conductivity, which is consistent with the results of Raman spectra.

The MA abilities of the prepared Co–ZnO–C and some absorbers reported recently are shown in Table 1. Co–ZnO–C has advantages in thin thickness and effective absorbing frequency band.
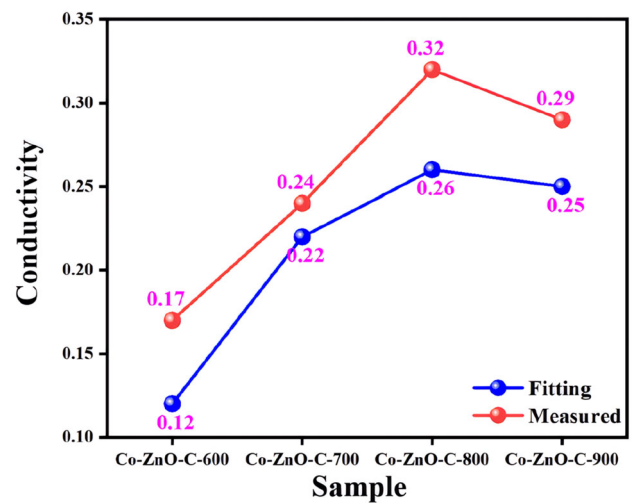

Fig. 9 The fitting and measured conductivity of Co–ZnO–C

Table 1 MA properties of related absorbers reported recently

Composite	Filling ratio (wt%)	Optimal RL value (dB)	f_m (GHz)	Matching thickness (mm)	Bandwidth thickness (mm)	Value (GHz)	Range (GHz)	Refs.
Co/C	40	− 58.5	5.8	4.7	1.7	5.40	12.30–17.70	[27]
Co/N-doped/C	25	− 52.5	13.1	3.0	2.2	4.40	11.96–15.36	[42]
Co/Co$_3$O$_4$/C	30	− 52.8	13.12	4.0	2.0–4.0	10.72	4.88–15.6	[33]
CoFe/C	25	− 44.1	4.08	5.8	2.3	5.20	9.70–14.9	[18]
Ni/ZnO/C	10	− 33.2	5.8	4.9	3.0	3.1	8.2–11.3	[6]
Co/ZnO/C	20	− 44.8	9.2	2.9	2.8	6.95	6.59–13.54	This work
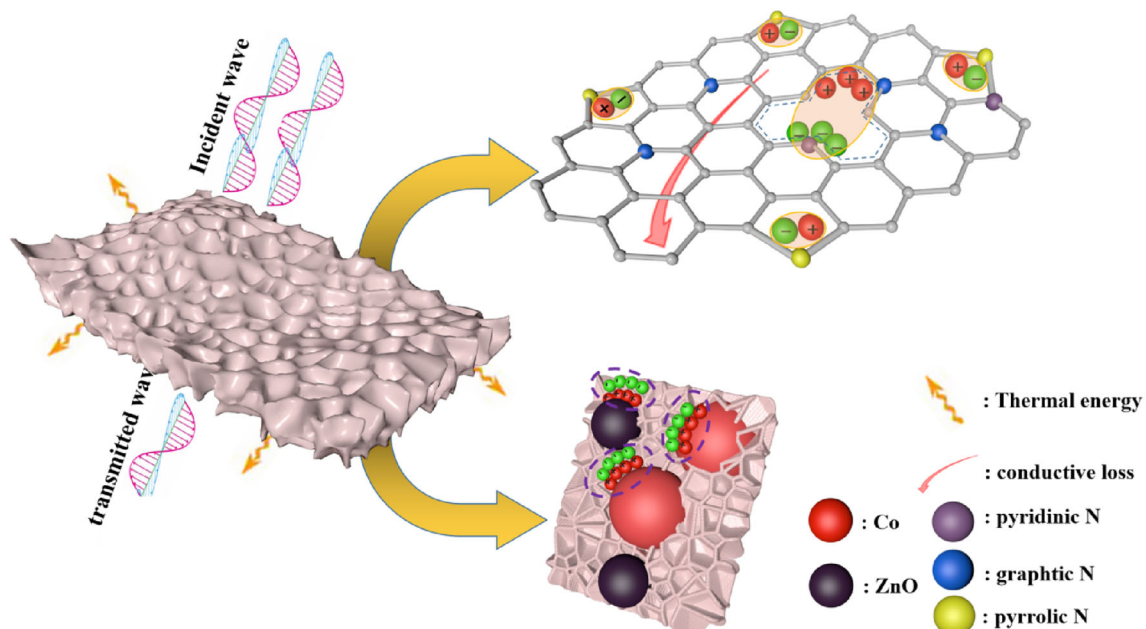
Fig. 10 Schematic illustration of the microwave dissipation mechanisms of Co–ZnO–C

As shown in Fig. 10, the possible microwave dissipation mechanisms of Co–ZnO-C are ascribed to the following aspects. A high-degree graphitic network with appropriate conductivity results in strong conductive loss. The interfaces of Co/C and ZnO/C offer significant interface polarization and Co causes magnetic loss simultaneously. Defects and electronegativity of nitrate atoms contribute to dielectric loss. Thus, the excellent microwave absorption ability of the Co–ZnO-C composites owes to the synergy of dielectric loss and magnetic loss.

4 Conclusion

To sum up, a facile strategy to synthesize the magnetic-semiconductor binary MOFs-based nanocomposites was proposed. The prepared Co–ZnO–C-800 sample exhibited excellent microwave dissipation ability, resulting from the multi-reflection in porous matrix and abundant polarization sites. The optimal RL of Co–ZnO–C-800 reached − 44.8 dB at 9.2 GHz in thickness of 2.9 mm, and the EAB was 6.95 GHz between 6.59 GHz and 13.54 GHz with the filler ratio of 20 wt%. Excellent EM wave absorption performance is attributed to synergy of multi-site

polarization relaxation, large conductance loss of MOFs derivative, and magnetic loss. The composite materials of porous carbon matrix combined with magnetic-semiconductor indicate a feasible strategy to prepare high-performance microwave absorbing materials.

Author contributions

Funding

Data availability

All data generated or analyzed during this study are included in this article.

Declarations

5. References

1. J. Liang, J. Chen, H. Shen, K. Hu, Chem. Mater. **33**, 1789–1798 (2021)
2. Y. Liu, Z. Chen, W. Xie, S. Song, ACS Sustain. Chem. Eng. **7**, 5318–5328 (2019)
3. L. Wang, M. Huang, X. Yu, W. You, Nanomicro Lett. **12**, 150 (2020)
4. T. Gao, Z. Zhu, Y. Li, H. Hu, Carbon **177**, 44–51 (2021)
5. M. Kong, X. Liu, Z. Jia, B. Wang, J. Colloid Interface Sci. **604**, 39–51 (2021)
6. Y. Lu, Y. Wang, H. Li, Y. Lin, ACS Appl. Mater. Interfaces **7**, 13604–13611 (2015)
7. Z. Wu, Z. Yang, K. Pei, X. Qian, Nanoscale **12**, 10149–10157 (2020)
8. Q. Hu, R. Yang, S. Yang, W. Huang, ACS Appl. Mater. Interfaces **14**, 10577–10587 (2022)
9. C. Liu, J. Wang, J.J. Wang, Z. Yu, Coord. Chem. Rev. **432**, 213743 (2021)
10. J.X. Wang, J.F. Yang, J. Yang, H. Zhang, Nanotechnology **31**, 394002 (2020)
11. L.Y. Wang, H. Xu, J.K. Gao, J.M. Yao, Coord. Chem. Rev. **398**, 213016 (2019)
12. X. Zhang, J. Qiao, Y. Jiang, F. Wang, Nanomicro Lett. **13**, 135 (2021)
13. L. Liu, Y. Duan, J. Guo, L. Chen, Phys. B: Condens. Matter **406**, 2261–2265 (2011)
14. H. Zhao, X. Xu, Y. Wang, D. Fan, Small **16**, 2003407 (2020)
15. S. Wei, T. Chen, Q. Wang, Z.C. Shi, J. Colloid Interface Sci. **593**, 370–379 (2021)
16. Q. Liao, M. He, Y. Zhou, S. Nie, ACS Appl. Mater. Interfaces **10**, 29136–29144 (2018)
17. W. Zhang, X. Yao, S. Zhou, X. Li, Small **14**, 1800423 (2018)
18. W.H. Gu, J.W. Tan, J.B. Chen, Z. Zhang, ACS Appl. Mater. Interfaces **12**, 28727–28737 (2020)
19. P. Liu, S. Gao, G. Zhang, Y. Huang, Adv. Funct. Mater. **31**, 2102812 (2021)
20. J. Tao, J. Zhou, Z. Yao, Z. Jiao, Carbon **172**, 542–555 (2021)
21. R.W. Shu, W.J. Li, Y. Wu, J.B. Zhang, Chem. Eng. J. **362**, 513–524 (2019)
22. L. Wang, X.Y. Bai, B. Wen, Z. Du, Compos. Part B-Eng. **166**, 464–471 (2019)
23. B.Y. Zhu, P. Miao, J. Kong, X.L. Zhang, Cryst. Growth. Des. **19**, 1518–1524 (2019)
24. L.N. Huang, S.L. Huang, Z.Y. Yang, A.L. Zhao, Nanomaterials **8**, 600 (2018)
25. X.H. Liang, B. Quan, G.B. Ji, W. Liu, ACS Sustain. Chem. Eng. **5**, 10570–10579 (2017)
26. Q.L. Wu, H.H. Jin, W. Chen, S.Q. Huo, Mater. Res. Express **5**, 065602 (2018)
27. P.B. Liu, S. Gao, Y. Wang, Y. Huang, ACS Appl. Mater. Interfaces **11**, 25624–25635 (2019)
28. H.L. Xu, X.W. Yin, M. Zhu, M.K. Han, ACS Appl. Mater. Interfaces **9**, 6332–6341 (2017)
29. W. Feng, Y.M. Wang, J.C. Chen, B.Q. Li, J. Mater. Chem. C **6**, 10–18 (2018)
30. J.T. Yuan, Q.C. Liu, S.K. Li, Y. Lu, Synth. Met. **228**, 32–40 (2017)

31. X. Liu, L.S. Wang, Y.T. Ma, Y.L. Qiu, Chem. Eng. J. **333**, 92–100 (2018)

32. X.Q. Cui, X.H. Liang, W. Liu, W.H. Gu, Chem. Eng. J. **381**, 122589 (2020)

33. K.F. Wang, S.Z. Zhang, W.S. Chu, H. Li, J. Colloid Interface Sci. **591**, 463–473 (2021)

34. J.Q. Tao, L.L. Xu, L. Wan, J.S. Hou, Nanoscale **13**, 12896–12909 (2021)

35. L. Wang, X.F. Yu, X. Li, J. Zhang, Chem. Eng. J. **383**, 122589 (2020)

36. B.H. Han, W.L. Chu, X.J. Han, P. Xu, Carbon **168**, 404–414 (2020)

37. Y. Li, X.F. Liu, X.Y. Nie, W.W. Yang, Adv. Funct. Mater. **29**, 1807624 (2019)

38. P.B. Liu, S. Gao, Y. Wang, Y. Huang, Chem. Eng. J. **381**, 122653 (2020)

39. Y. Qiu, Y. Lin, H.B. Yang, L. Wang, Chem. Eng. J. **383**, 123207 (2020)

40. G.Z. Shen, Y.W. Xu, B. Liu, P. Du, J. Alloys Compd. **680**, 553–559 (2016)

41. H.L. Xu, X.W. Yin, Z.C. Li, C.L. Liu, Nanotechnology **29**, 184003 (2018)

42. L.J. Yang, T.W. Deng, Z.R. Jia, X.D. Zhou, J. Mater. Sci. Technol. **83**, 239–247 (2021)

43. P.J. Liu, V.M.H. Ng, Z.J. Yao, J.T. Zhou, ACS Appl. Mater. Interfaces **9**, 16404–16416 (2017)

44. AharoniAmikam, J. Appl. Phys. **69**, 7762–7764 (1991)

45. J. Ouyang, Z.L. He, Y. Zhang, H.M. Yang, ACS Appl. Mater. Interfaces **11**, 39304–39314 (2019)

46. Y.H. Wang, X.D. Li, X.J. Han, P. Xu, Chem. Eng. J. **387**, 124–159 (2020)

47. Z.M. Man, P. Li, D. Zhou, Y.Z. Wang, Nano Lett. **20**, 3769–3777 (2020)